Robust topological temperature localization in thermal rock-paper-scissors chain

Zhaochen Wang[1], Quan Liu[1], Xin Qian[1], Xiaobing Luo[1], Run Hu[1,2,3,4,*]

[1]School of Energy and Power Engineering, Huazhong University of Science and Technology, Wuhan 430074, China

[2]State Key Laboratory of High-Density Electrical Energy Conversion, Huazhong University of Science and Technology, Wuhan 430074, China

[3]Department of Applied Physics, Kyung Hee University, Yongin-Si 17104, Korea

[4]Shenzhen Institute of Huazhong University of Science and Technology, Shenzhen 518052, China

[*]Corresponding author. E-mail: hurun@hust.edu.cn

ABSTRACT: Emerging topological thermal physics has revolutionized thermal management with topological thermal metamaterials, but most of them only consider the passive/static thermal diffusion. Inspired by ecological dynamics, we investigate the topological thermal physics in an active/dynamic three-body heat transfer system connected with Peltier modules, where the cyclic interaction is exemplified by the rock-paper-scissors (RPS) chain. Numerical simulations demonstrate a robust temperature localization phenomenon against parametric disturbance and structural perturbations, and topological phase transition in thermal RPS chain is discussed via topological band theory analysis of the corresponding Hamiltonian. Our findings establish a framework for exploring dynamic topological phenomena in non-equilibrium thermal transport, offering new pathways for active thermal management.

INTRODUCTION

Inspired by topological photonics and topological acoustics [1–7], the counterpart topological thermal transport, enabled by thermal metamaterials [8–14], emerges as a groundbreaking research paradigm beyond the traditional heat transfer, and significantly reshapes the way we think about and deal with heat and advances the thermal management technologies like thermal shielding/cloaking and harvesting/concentrating devices [15–25]. Under such physical framework, a lot of topological thermal physics are reported such as nonreciprocal/asymmetric heat transfer [26–28], skin effect [29,30], geometrical phase [31–33], protected edge

state [34,35], bulk-boundary correspondence [36–38], and so on. However, most of them only consider the passive/static thermal diffusion, can we observe more thermal physics in active/dynamic systems?

Recently, the active topological phase transition system in active matter [39–41], fluid dynamics [42,43], and ecological systems [44–47] have started to develop, but a counterpart thermal physics in such systems remains underexplored. A typical ecological system is the population dynamics that studies how the number of individuals in a population changes over time, affected by factors such as birth, death, predation, and competition. Real ecological systems are extremely complex, with numerous species and intricate interactions. Under specific situations, the population dynamics can be simplified to only consider the interactions among three species, such as communities containing toxin-producing *E. coli* [48,49], the competition among cryptic coral reefs [50], and the reproductive strategies of the side-blotched lizards [51]. Due to predation and competition, the population of such three species will be dynamically balanced and can be modeled by the rock-paper-scissors (RPS) cycle. Take the side-blotched lizards with different colored stripes as an example. Orange males (analogous to "rock"), characterized by aggression, overpower blue males through physical superiority and expansive harems. Blue males (analogous to "scissors"), with smaller territories and heightened vigilance, effectively counter yellow males that mimic females and steal mating opportunities. Yellow males (analogous to "paper"), counter orange males by stealthily infiltrate their territories and steal mating opportunities [Fig. 1(a) and (b)]. Such RPS model describes the cyclic competition in a lot of systems ranging from biodiversity in ecosystems [48–51] to phase transitions in non-equilibrium quantum systems [44–46]. Recent advances in topological physics have revealed that such RPS cyclic interactions can encode geometric phases and protected edge modes in synthetic lattices [44,45]. Can we extend such RPS model to describe active/dynamic thermal physics beyond passive/static thermal diffusion?

In this letter, inspired by RPS cycle in ecological systems, we establish an actively-regulated three-body heat transfer system connected with Peltier modules to mimic the RPS cyclic interactions [Fig. 1(c)], and extend the RPS cycles into a RPS chain to explore the topological physics of thermal transport. Robust temperature localization due to the heat accumulation is found in the RPS chain and the topological phase transition are analyzed through energy band theory.

RESULTS

Generation of thermal RPS chain

To implement the RPS model in thermal diffusion systems, we connect three body via Peltier modules and the whole system is assumed with the same material and

structure [Fig. 1(d)]. Heat transfer between every two bodies consists of intrinsic thermal diffusion (proportional to the temperature gradient) and Peltier heating/cooling power (proportional to the average temperature). We then connect a series of RPS cycles into a RPS chain, and each unit cell consists of two thermal sites (A and B). The heat flow through the Peltier module is at a rate of $Q = SIT_{\mathrm{avg}}$, where S, I, and T_{avg} are the Seebeck coefficient, the electric current, and the average temperature of the channel. The heat flow direction depends on the direction of the current. In each PRS cycle, as shown in Fig. 1b, the active transport coefficients of the three channels are P_1, P_2, and P_3 respectively, and the corresponding intrinsic diffusion coefficients are D_1, D_2, and D_3 respectively (detailed in Supplemental Note I). By discretizing the heat transfer equations in the RPS chain, we can obtain the governing equations of the temperature field as

$$\begin{cases} \dfrac{\partial T_{n,A}}{\partial t} = D_1\left(T_{n+1,A} - T_{n,A}\right) + D_1\left(T_{n-1,A} - T_{n,A}\right) \\ \qquad + D_2\left(T_{n-1,B} - T_{n,A}\right) + D_3\left(T_{n,B} - T_{n,A}\right) \\ \qquad + P_3\left(T_{n,B} + T_{n,A}\right) + P_1\left(T_{n-1,A} + T_{n,A}\right) \\ \qquad - P_2\left(T_{n-1,B} + T_{n,A}\right) - P_1\left(T_{n+1,A} + T_{n,A}\right) \\ \dfrac{\partial T_{n,B}}{\partial t} = D_2\left(T_{n+1,A} - T_{n,B}\right) + D_3\left(T_{n,A} - T_{n,B}\right) \\ \qquad + P_2\left(T_{n+1,A} + T_{n,B}\right) - P_3\left(T_{n,A} + T_{n,B}\right) \end{cases}, \tag{1}$$

where $T_{\mathrm{n,A}}$ and $T_{\mathrm{n,B}}$ denote the temperature of site A and B in unit n. The discretized RPS chain system yields an effective Hamiltonian for the site-channel model, establishing a thermal analog (antisymmetrice Hamiltonian) to the RPS mass-conserving dynamical system (detailed derivation in Supplemental Note I). Eq. (1) can be articulated as $\partial_t \hat{\mathbf{T}} = -i\mathbf{H}\hat{\mathbf{T}}$, where $\hat{\mathbf{T}} = \begin{bmatrix} T_{1,A} & T_{1,B} & \cdots & T_{n,B} \end{bmatrix}^T$ represents the temperature field of whole RPS chain, $\mathbf{H}$ corresponds to the Hamiltonian operator and i is the imaginary unit. For theoretical analysis with periodic boundary conditions (PBC), we close the chain by coupling the last B site back to the first A site, forming a ring with an even total number of sites $s = 2N$, where N is the total number of units. For open boundary conditions (OBC) used in most situations, the chain is terminated, resulting in an odd total number of sites $s = 2N+1$ (see detailed discussion with boundary conditions in Supplemental Note IV). Consider an OBC thermal RPS chain, the corresponding Hamiltonian can be written as

$$\mathbf{H}=(-i)\cdot\begin{bmatrix} D_1+D_3+P_1-P_3 & -D_3-P_3 & -D_1+P_1 & \cdots & & & \\ -D_3+P_3 & D_2+D_3+P_3-P_2 & -D_2-P_2 & \cdots & & & \\ -D_1-P_1 & -D_2+P_2 & 2D_1+D_2+D_3+P_2-P_3 & -D_3-P_3 & -D_1+P_1 & \cdots & \\ \vdots & \vdots & -D_3+P_3 & D_2+D_3+P_3-P_2 & -D_2-P_2 & \cdots & \\ & & \vdots & \vdots & \ddots & \vdots & \vdots \\ & & & \cdots & -D_3+P_3 & D_2+D_3+P_3-P_2 & -D_2-P_2 \\ & & & \cdots & -D_1-P_1 & -D_2+P_2 & D_1+D_2+P_2-P_1 \end{bmatrix}. \quad (2)$$

Without loss of generality, we assume $P_1 = P_3$ and define $R = P_2 / P_3$ as the skewness parameter for exploring the thermal energy dynamics. The RPS chain can be thought of as a one-dimensional chain of nonlinear oscillators because each isolated RPS cycle represents a local oscillator in which heat oscillates between the different sites. When $P_j >> D_j$ (j = 1,2,3), thus D_j in the Hamiltonian can be neglected, and the Hamiltonian H becomes antisymmetric (see Supplemental Note I for details). When D_j and P_j are at the same order of magnitude, both will influence the topological properties significantly. In the following, intricate temperature distribution patterns depending on the skewness parameter R are revealed.

Temperature localization and robustness in thermal RPS chain

For skewness $R < 1$, more thermal energy is moved to the right due to the smaller P_2 in the RPS cycle, resulting in the maximum temperature in the right boundary of the RPS chain, which corresponds to the progressive polarization toward the right boundary over time regardless of the initial conditions [Fig. 2(a)]. Conversely for $R > 1$, more thermal energy is moved to the left and a left-boundary polarization emerges [Fig. 2(c)]. For $R = 1$, there is no-biased net thermal energy and the temperature field preserves homogeneity across the whole chain [Fig. 2(b)]. This temperature localization becomes manifest as a decay of the average temperature per site along the chain direction. We quantify this polarization by evaluating the average temperature of each site. The temperature profile exhibits a jagged pattern, alternating between A and B sites. When examined separately, the temperatures of A sites across different units show a consistent gradient, as do the B sites [Fig. 2(d-f)]. Such localization arises for any initial temperature distribution and is intuitively demonstrated in a finite system (s = 13). Remarkably, the skewness R exclusively determines whether the overall temperature field polarizes to the left or right boundaries of the chain, while the values of other parameters only influence the temperature values but not the direction of localization.

Although the governing Hamiltonian **H** is derived from the transient equation [Eq. (1)], the temperature distribution of the thermal RPS model eventually evolves toward a steady state after a certain period of time. To further investigate the transient temperature characteristic of the thermal RPS chain, the initial temperature of each site is set to the reference temperature (T_0 = 293.15 K). Fig. 2(g-i) illustrate the transient temperature distribution with skewness R = 0.5, 1 and 2. When $R \neq 1$, a temperature localization effect emerges and strengthens over time. The direction of this localization

remains consistent with the steady-state profile, while its magnitude increases progressively, starting from an initially uniform distribution and eventually converging to the final steady state. When R = 1, the heat transfer between each site forms a dynamic equilibrium. Therefore, the temperature remains constant at the initial value.

We quantify the temperature localization by calculating the temperature-weighted geometric center $\overline{x}_T = \int_0^L xT(x)dx \Big/ \int_0^L T(x)dx$, where L is the total length of thermal RPS chain (see Supplemental Note II for details). When R = 1, the temperature is uniform and thus $\overline{x}_T$ coincides with the real geometric center $\overline{x}_g = L/2$ of the RPS chain. In contrast, $\overline{x}_T$ shifts from $\overline{x}_g$ when R varies, which could be used for characterizing the temperature localization. When $R < 1$, $\overline{x}_T > \overline{x}_g$, indicating that the overall temperature undergoes polarization to the right. When $R > 1$, $\overline{x}_T < \overline{x}_g$, indicating that the overall temperature undergoes polarization to the left. The greater the $\overline{x}_T$ deviates from $\overline{x}_g$, the greater the polarization strength will be.

The above temperature localization demonstrates exceptional robustness against both parametric disturbance and structural perturbations. Figs. 3a-3c illustrate the polarization of temperature to the boundary when the active transport coefficient are perturbed as $P_i = P_i(1+\varepsilon_i)$, where P_i is the active transport coefficient of the i-th channel, and the perturbation ε_i are randomly chosen within the set of $\{\varepsilon_i | -0.2 < \varepsilon_i < 0.2\}$. It is seen that the states of temperature localization are not affected by the perturbation ε_i with different R, indicating the great robustness against the disturbance. On the other hand, the temperature localization also remains robust when extra coupling between each site B is introduced, just as the predator-herbivore relationships in nature are affected by external influences. Specifically, extra channels between each site B are added to the RPS chain with an active transport coefficient $P_4 = \varepsilon \cdot P_1$ [Fig. 3(d-f)]. These incorporating additional couplings (ε = 0.3) fail to disrupt the fundamental qualitative temperature localization direction.

Topological phase transition and Topological Band Theory

For R = 1, thermal energy is uniformly distributed along the chain and the temperature is homogeneous. Otherwise, any change in R will cause the temperature of the entire system to start polarization and eventually lead to a new state of localization. More generally, from our following calculations it turns out that it is not possible to tune any set of active transport coefficients on the RPS chain such that one passes from

localization at one boundary to the other boundary without crossing a transition point at $R = 1$. Further research in the topological band theory will also support this view as follows.

To further characterize the topological properties of RPS chain, we apply PBC for calculating the Bloch Hamiltonian as

$$\mathbf{H}(k)=(-i)\begin{bmatrix}(2D_1+D_2+D_3-P_3+P_2)-(D_1-P_1)e^{ik}-(D_1+P_1)e^{-ik} & -(D_3-P_3)-(D_2+P_2)e^{ik}\\ -(D_3+P_3)-(D_2-P_2)e^{-ik} & D_2+D_3-P_2+P_3\end{bmatrix}, \quad (3)$$

where k is the wavenumber in the Brillouin zone (BZ), defined as $\beta=e^{ik}$, $k\in(-\pi, \pi]$. When $P_j >> D_j$, we ignore the diffusion coefficient D_j and the Hamiltonian is simplified as

$$\mathbf{H}(k)=(-i)\begin{bmatrix}P_2-P_3+P_1e^{ik}-P_1e^{-ik} & P_3-P_2e^{ik}\\ -P_3+P_2e^{-ik} & P_3-P_2\end{bmatrix}. \quad (4)$$

In non-Hermitian systems, conventional BZ fails to correctly predict the spectrum and topological characteristic under OBC [5,52]. In order to analyze the topological localization phenomena, the non-Hermitian Bloch vector should be extended to complex domain to recover the breakdown of bulk-boundary correspondence. This implies that the usual Bloch phase factor e^{ik} is generalized to $\beta = e^{ik'} = re^{ik}$ and the wavenumber acquires an imaginary part: $k \rightarrow k' = k - i\ln r$. The legitimate values of β trace out a trajectory in the complex plane, known as the generalized Brillouin zone (GBZ). The corresponding GBZ Hamiltonian is given by:

$$\mathbf{H}(\beta)=(-i)\begin{bmatrix}P_2-P_3+P_1\beta-P_1\beta^{-1} & P_3-P_2\beta\\ -P_3+P_2\beta^{-1} & P_3-P_2\end{bmatrix}. \quad (5)$$

The precise shape of GBZ can be found as follows. From the eigenvalue function $\det[H(\beta)-EI]=0$, a given E corresponds to two β roots denoted as $\beta_1(E)$ and $\beta_2(E)$, then the solution of equation $\beta_1(E) = \beta_2(E)$ determines the legitimate values of E and β. These values of β form a continuous contour in the complex plane which is GBZ and the corresponding eigenvalues E are obtained to analyze the band structure and topological properties of the RPS chain.

Figure 4(d) illustrates the GBZ with skewness $R = 0.5$, 1 and 2. For skewness $R=1$, GBZ is degenerated into BZ, which is a unit circle. For $R<1$, GBZ constitutes a continuous contour lying entirely outside the unit circle. Conversely for $R>1$, the contour lies entirely inside the unit circle. In all cases, the GBZ is not circular but a continuous curve symmetric about the real axis [$\mathrm{Im}(\beta)=0$] except for $R = 1$. The band structures of thermal RPS chain in GBZ are depicted in Fig. 4(a-c) and 4(e-g), where the horizontal axis is the argument $arg(\beta)$. Here, $arg(\beta) = \mathrm{Re}(k')$, which represents the real part of the complex wave-vector in the GBZ framework. The real part $\mathrm{Re}(E)$ [Fig.

4(a-c)] and imaginary part Im(E) [Fig. 4(e-g)] of eigenvalue of $\mathbf{H}(\beta)$ represent the transmission and the dissipation of thermal energy respectively. First, the spectrum of Re(E) exhibits two bands of eigenvalues on the GBZ, reflecting the two sides A and B of a unit. For $R = 1$, the two branches intersect at $arg(\beta) = 0$, whereas for $R \neq 1$, they are separated by a spectral gap. This gap closes only for $R = 1$ at $arg(\beta) = 0$, supporting the view that $R = 1$ is the only critical point for topological phase transition. Secondly, a clear transition is also observed in Im(E). For $R = 1$, $\mathbf{H}(\beta)$ is Hermitian, and all eigenvalues are pure real, denoting the thermal dissipative behavior only. In contrast, for $R \neq 1$, Im(E) presents a distribution with axial symmetry, and the band branches intersect at $arg(\beta) = 0$. This marked change in the imaginary band structure across the critical point $R = 1$ further corroborates the occurrence of a phase transition.

Since the eigenenergy spectrum collapses into an arc in GBZ (detailed comparison between BZ and GBZ in Supplemental Note III), the topological invariant (winding number W) is calculated in BZ as

$$W = \frac{1}{2\pi}\oint_{BZ}\frac{d}{dk}\arg\left[H(k) - E_b\right]dk, \tag{6}$$

where E_b is the reference point. Essentially, W gives the number of times the complex eigenenergy encircles E_b. This topological invariant W serves as an indicator of the topological phase of thermal RPS chain. The relationship between W and the skewness R are shown in Fig. 4(h). $W = -1$ and $+1$ correspond to temperature localization toward the right ($R < 1$) and left ($R > 1$) respectively. A topological phase transition occurs at $R = 1$ and these two phases ($R < 1$ and $R > 1$) are topologically distinct, as one cannot be deformed into the other without crossing critical point.

The eigenvalues λ and eigenvectors of the OBC Hamiltonian for a finite thermal RPS chain provide further evidence of the phase transition. The Hamiltonian follows the form given in Eq. (S9) and the results are illustrated in Fig. 5(a) ($s = 81$). As R increases across the critical value $R = 1$, the two spectral branches exhibit a reversal in their opening direction. The branch of $R < 1$ opens upward while the branch of $R > 1$ opens downward. Moreover, an obvious gap emerges at $\lambda = 0$ if $R \neq 1$. This zero point corresponds to an eigenmode where both propagation [Re(λ)=0] and dissipation [Im(λ)=0] cease, indicating the steady state of the thermal RPS chain. The associated eigenvector is thus referred to as the steady-state eigenvector. Further investigation of the steady-state eigenvector is presented in Fig. 5(b) ($s = 13$). As for $R < 1$, the steady-state eigenvectors localize toward the left (the region with the smaller N), with the degree of localization becoming more pronounced as R decreases. Conversely for $R > 1$, the localization occurs toward the right (larger N), strengthening as R increases. At $R = 1$, the eigenvectors are uniformly distributed across all sites. This spatial localization behavior aligns fully with the observed temperature localization patterns. It is worth noting that this localization is different from reported thermal skin effect [29,30], which

focuses more on the temperature distribution / eigenvectors during transient processes, while we are more concerned with the steady state. This is because reported thermal skin effect is a purely passive dissipation process, under adiabatic boundary conditions, heat will inevitably evolve toward a uniform distribution. While in our model, due to the active thermal control driven by thermoelectric materials, the temperature field evolves from an initial distribution and continuously accumulates toward a certain direction, eventually forming a stable temperature localization profile. To quantitatively characterize this localization, we introduce the inverse participation ratio (IPR), defined as $IPR = \sum |\phi_i|^4$, where ϕ_i denotes the amplitude at site *i*. Large IPR usually corresponds to localization. Fig. 5(c) shows the normalized temperature deviation and IPR under steady state with *R* varying from 0.5 to 2. At *R* = 1, the normalized temperature deviation changes sign and the IPR reaches its minimum. These two indicators jointly indicate that the localization of temperature and the localization of the steady-state eigenvector are highly consistent in both direction and magnitude. The agreement between topological band theory and actual heat transport behavior strongly supports the existence of a topological phase transition in the thermal RPS chain.

DISCUSSION AND CONCLUSION

Inspired by the cyclic restraint relationships among biological populations in nature, we establish a thermal RPS chain and investigate the robust temperature localization and topological phase transition with both phenomenology and topological band theory analysis. The influence of the skewness parameter *R* on the direction of temperature localization is analyzed, as well as the robustness of thermal RPS chain under parameter and structural perturbations. Further, the topological phase transition that occurs at *R* = 1 in thermal RPS chain is clarified with both temperature localization phenomena and band structure analysis. Owing to the progress on high-efficiency thermoelectric materials and three-dimensional printing, thermal RPS chain's ability to robustly steer and localize heat to a designated boundary on demand has become possible. This work successfully establishes a non-equilibrium thermal transport model at the macroscopic level, laying the foundation for more topological thermal transfer phenomena and paving ways for potential advanced thermal management technologies.

METHODS

The robust topological temperature localization in thermal rock-paper-scissors chain is verified by the finite element simulations. In the simulation, we construct the OBC model consists of 13 sites (*N* = 6) as shown in Fig. 2. The distance between each

site is 30 mm. The material is set as copper with thermal conductivity κ = 400 $W\cdot m^{-1}\cdot K^{-1}$, density $\rho = 8.9\times10^3$ $kg\cdot m^{-3}$, and capacity c = 390 $J\cdot kg^{-1}\cdot K^{-1}$. The initial temperature is set as 293.15 K and the boundary condition is set as adiabatic. The simulated results are shown in Figs. 2 and 3.

SUPPLEMENTARY DATA

Supplementary data are available at NSR online.

FUNDING

This work was supported by the National Key Research and Development Program of China (2024YFB4104701 and 2022YFA1203104), the National Natural Science Foundation of China (52422603, 52511540065, 52521008, W2521166 and 92463311), the Science and Technology Program of Hubei Province (2023AFA072), the Interdisciplinary Research Program of HUST (5003120094), the Shenzhen Technology Project (JCYJ20241202123700001) and the Open Research Fund of Suzhou Laboratory (SZLAB-1508-2024-TS016).

AUTHOR CONTRIBUTIONS

Z.W. and R.H. conceived the idea. Z.W., Q.L. and R.H. proposed the methodology. Z.W. and Q.L. performed the theoretical derivation. Z.W., Q.L. and R.H. made the visualizations. Z.W., X.Q., X.L. and R.H. performed the theoretical analysis and wrote the manuscript. R.H. supervised the work. All authors contributed to the discussion and finalization of the manuscript.

COMPETING INTERESTS

The authors declare no competing interests.

REFERENCES

1. Li M, Zhirihin D and Gorlach M *et al*. Higher-order topological states in photonic kagome crystals with long-range interactions. *Nat Photonics* 2020; **14**: 89–94.
2. Benalcazar WA, Bernevig BA and Hughes TL. Quantized electric multipole insulators. *Science* 2017; **357**: 61–6.
3. Guo J, Gu Z and Zhu J. Realization of merged topological corner states in the continuum in acoustic crystals. *Phys Rev Lett* 2024; **133**: 236603.
4. Fleury R, Sounas DL and Sieck CF *et al*. Sound isolation and giant linear nonreciprocity in a compact acoustic circulator. *Science* 2014; **343**: 516–9.
5. Zhang X, Zhang T and Lu M-H *et al*. A review on non-Hermitian skin effect. *Adv Phys-X* 2022; **7**: 2109431.
6. El-Ganainy R, Makris KG and Khajavikhan M *et al*. Non-Hermitian physics and PT symmetry. *Nat Phys* 2018; **14**: 11–9.
7. Weidemann S, Kremer M and Helbig T *et al*. Topological funneling of light. *Science* 2020; **368**: 311–4.
8. Liu Z, Jin P and Lei M *et al*. Topology in thermal, particle, and plasma diffusion metamaterials. *Chem Rev* 2025; **125**: 8655–730.
9. Jin P, Wang C and Zhou Y *et al*. Temporal anti-parity–time symmetry in diffusive transport. *Nat Phys* 2026; **22**: 195–201.
10. Zhuang P, Wang C and Yang F *et al*. Rescaled Schwarz–Christoffel transformations for isotropic, polygon, and multiphysics metamaterials. *Phys Rev Lett* 2025; **135**: 216901.
11. Fan CZ, Gao Y and Huang JP. Shaped graded materials with an apparent negative thermal conductivity. *Appl Phys Lett* 2008; **92**: 251907.
12. Liu Q, Wang Z and Kim S-K *et al*. Remote spatiotemporal control of local states in thermal lattice. *Mater Today Phys* 2025; **59**: 101954.
13. Wang Z, Liu Q and Xiang L *et al*. Macroscale anomalous heat conduction in active thermal metamaterials. *Newton* 2025; **1**: 100255.
14. Li Y, Xu L and Qiu C-W. *Thermal metamaterials: controlling the flow of heat*. Singapore: World Scientific, 2025.
15. Yang F, Zhang Z and Xu L *et al*. Controlling mass and energy diffusion with metamaterials. *Rev Mod Phys* 2024; **96**: 015002.
16. Sha W, Xiao M and Zhang J *et al*. Robustly printable freeform thermal metamaterials. *Nat Commun* 2021; **12**: 7228.
17. Wang Z, Zhu Z and Liu T *et al*. Inverse design of thermal metamaterials with holey engineering strategy. *J Appl Phys* 2022; **132**: 145102.
18. Zhu Z, Wang Z and Liu T *et al*. Arbitrary-shape transformation multiphysics cloak

by topology optimization. *Int J Heat Mass Transfer* 2024; **222**: 125205.
19. Zhu Z, Ren X and Sha W *et al*. Inverse design of rotating metadevice for adaptive thermal cloaking. *Int J Heat Mass Transfer* 2021; **176**: 121417.
20. Sha W, Hu R and Xiao M *et al*. Topology-optimized thermal metamaterials traversing full-parameter anisotropic space. *Npj Comput Mater* 2022; **8**: 179.
21. Xu H, Shi X and Gao F *et al*. Ultrathin three-dimensional thermal cloak. *Phys Rev Lett* 2014; **112**: 054301.
22. Hu R, Xi W and Liu Y *et al*. Thermal camouflaging metamaterials. *Mater Today* 2021; **45**: 120–41.
23. Narayana S and Sato Y. Heat flux manipulation with engineered thermal materials. *Phys Rev Lett* 2012; **108**: 214303.
24. Hu R, Zhou S and Li Y *et al*. Illusion thermotics. *Adv Mater* 2018; **30**: 1707237.
25. Hu R, Huang S and Wang M *et al*. Encrypted thermal printing with regionalization transformation. *Adv Mater* 2019; **31**: 1807849.
26. Li J, Li Y and Cao P-C *et al*. Reciprocity of thermal diffusion in time-modulated systems. *Nat Commun* 2022; **13**: 167.
27. Xu L, Xu G and Huang J *et al*. Diffusive Fizeau drag in spatiotemporal thermal metamaterials. *Phys Rev Lett* 2022; **128**: 145901.
28. Ju R, Cao P and Wang D *et al*. Nonreciprocal heat circulation metadevices. *Adv Mater* 2024; **36**: 2309835.
29. Liu Y-K, Cao P-C and Qi M *et al*. Observation of non-Hermitian skin effect in thermal diffusion. *Sci Bull* 2024; **69**: 1228–36.
30. Cao P-C, Li Y and Peng Y-G *et al*. Diffusive skin effect and topological heat funneling. *Commun Phys* 2021; **4**: 230.
31. Qi M, Wang D and Cao P *et al*. Geometric phase and localized heat diffusion. *Adv Mater* 2022; **34**: 2202241.
32. Xu G, Li Y and Li W *et al*. Configurable phase transitions in a topological thermal material. *Phys Rev Lett* 2021; **127**: 105901.
33. Xu G, Yang Y and Zhou X *et al*. Diffusive topological transport in spatiotemporal thermal lattices. *Nat Phys* 2022; **18**: 450–6.
34. Liu Z, Cao P-C and Xu L *et al*. Higher-order topological in-bulk corner state in pure diffusion systems. *Phys Rev Lett* 2024; **132**: 176302.
35. Wang Z, Liu T and Zhu Z *et al*. Periodicity alters topological states in thermal diffusion system. *Int J Heat Mass Transfer* 2024; **235**: 126182.
36. Wu H, Hu H and Wang X *et al*. Higher-order topological states in thermal diffusion. *Adv Mater* 2023; **35**: 2210825.
37. Hu H, Han S and Yang Y *et al*. Observation of topological edge states in thermal diffusion. *Adv Mater* 2022; **34**: 2202257.

38. Yoshida T and Hatsugai Y. Bulk-edge correspondence of classical diffusion phenomena. *Sci Rep* 2021; **11**: 888.
39. Liu F and Wakabayashi K. Novel topological phase with a zero Berry curvature. *Phys Rev Lett* 2017; **118**: 076803.
40. Shankar S, Souslov A and Bowick MJ *et al*. Topological active matter. *Nat Rev Phys* 2022; **4**: 380–98.
41. Fruchart M, Hanai R and Littlewood PB *et al*. Non-reciprocal phase transitions. *Nature* 2021; **592**: 363–9.
42. Zhao S, Tian Z and Shen C *et al*. Topological acoustofluidics. *Nat Mater* 2025; **24**: 707–15.
43. Liu Q, Wang Z and Zeng M *et al*. Dynamically adjustable topological edge states in thermal diffusion-advection system. *Fundamental Res* 2025, doi: 10.1016/j.fmre.2025.02.001.
44. Knebel J, Geiger PM and Frey E. Topological phase transition in coupled rock-paper-scissors cycles. *Phys Rev Lett* 2020; **125**: 258301.
45. Yoshida T, Mizoguchi T and Hatsugai Y. Chiral edge modes in evolutionary game theory: A kagome network of rock-paper-scissors cycles. *Phys Rev E* 2021; **104**: 025003.
46. Felski A and Kunst FK. Exceptional points and stability in nonlinear models of population dynamics having PT symmetry. *Phys Rev Res* 2025; **7**: 013326.
47. Liang J, Dai Q and Li H *et al*. Topological phases in population dynamics with rock-paper-scissors interactions. *Phys Rev E* 2024; **110**: 034208.
48. Kerr B, Riley MA and Feldman MW *et al*. Local dispersal promotes biodiversity in a real-life game of rock–paper–scissors. *Nature* 2002; **418**: 171–4.
49. Kirkup BC and Riley MA. Antibiotic-mediated antagonism leads to a bacterial game of rock–paper–scissors in vivo. *Nature* 2004; **428**: 412–4.
50. Buss LW and Jackson JBC. Competitive networks: Nontransitive competitive relationships in cryptic coral reef environments. *Am Nat* 1979; **113**: 223–34.
51. Sinervo B and Lively CM. The rock–paper–scissors game and the evolution of alternative male strategies. *Nature* 1996; **380**: 240–3.
52. Zhang K, Yang Z and Fang C. Correspondence between winding numbers and skin modes in non-Hermitian systems. *Phys Rev Lett* 2020; **125**: 126402.

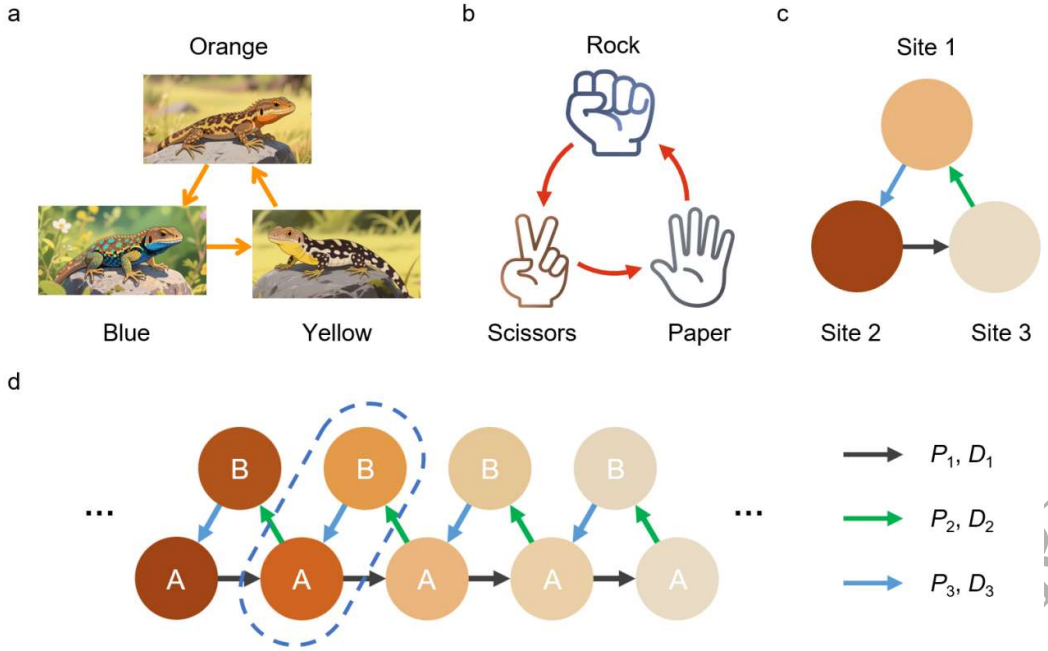

Figure 1. Schematic of thermal RPS chain. (a) Mutually restrictive relationships of three typical species of side-blotched lizards with orange-, blue-, and yellow-colored stripes. (b) Rock-Paper-Scissors Game. (c) Thermal RPS cycle with different active transport coefficient P_j and thermal diffusion coefficient D_j. (d) Structure of thermal RPS chain connected by a series of RPS cycles. Thermal sites A and B can be regarded as one unit cell.

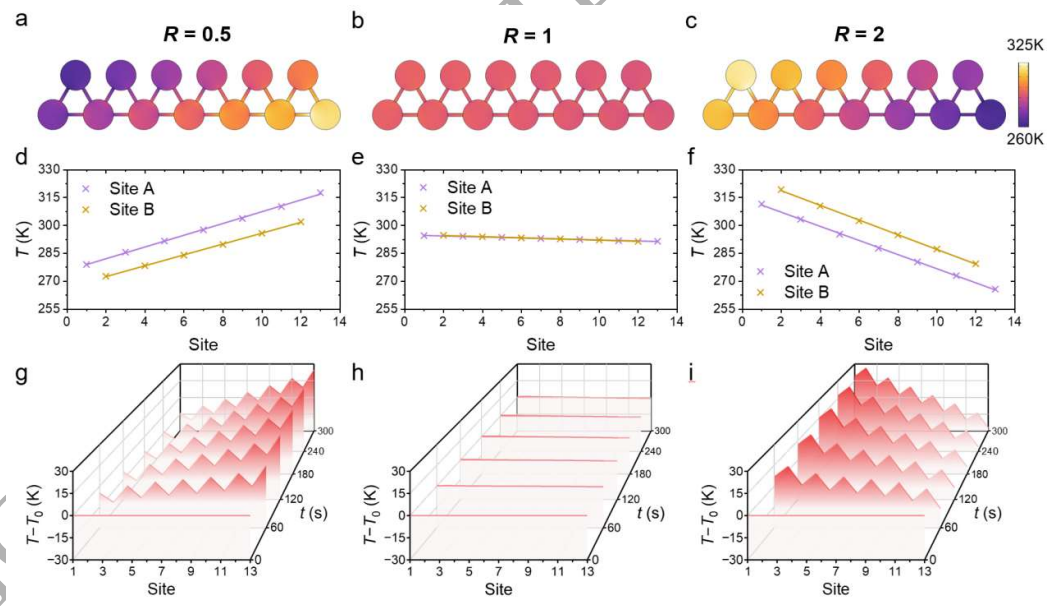

Figure 2. Temperature localization in thermal RPS chain (s = 13). (a-c) Temperature

distribution of thermal PRS chain with skewness R = 0.5, 1 and 2. (d-f) Steady-state temperature of sites A and B in thermal PRS chain with skewness R = 0.5, 1 and 2. (g-i) Transient temperature change of each site in thermal PRS chain with skewness R = 0.5, 1 and 2.

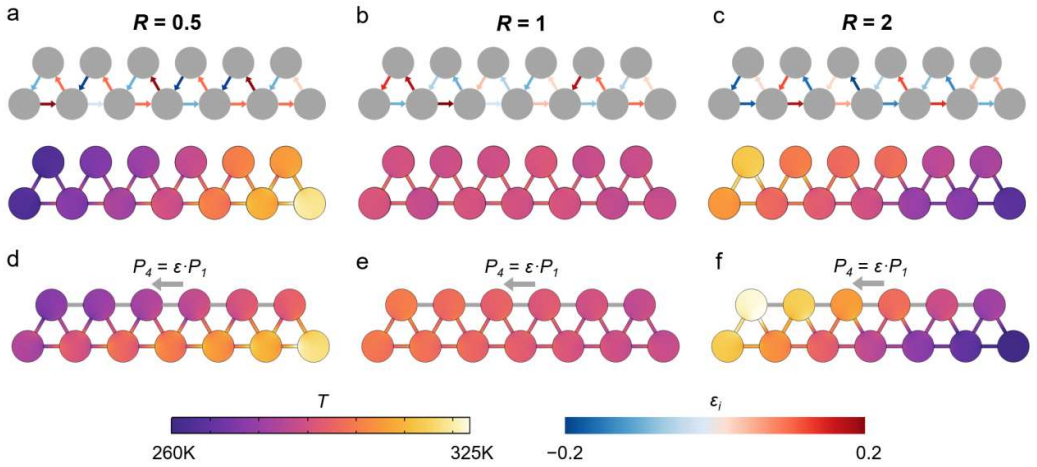

Figure 3. Robustness of temperature localization in thermal RPS chain. (a-c) Applied disturbance on active transport coefficient $P_n = P_n(1+\varepsilon_n)$ and the corresponding temperature distribution. The perturbation coefficient ε_n is denoted with the color of the channel. (d-f) Structural perturbations and extra couplings with active transport coefficient $P_4 = \varepsilon \cdot P_1$ and the corresponding temperature distribution. The structural perturbations are denoted with gray channels.

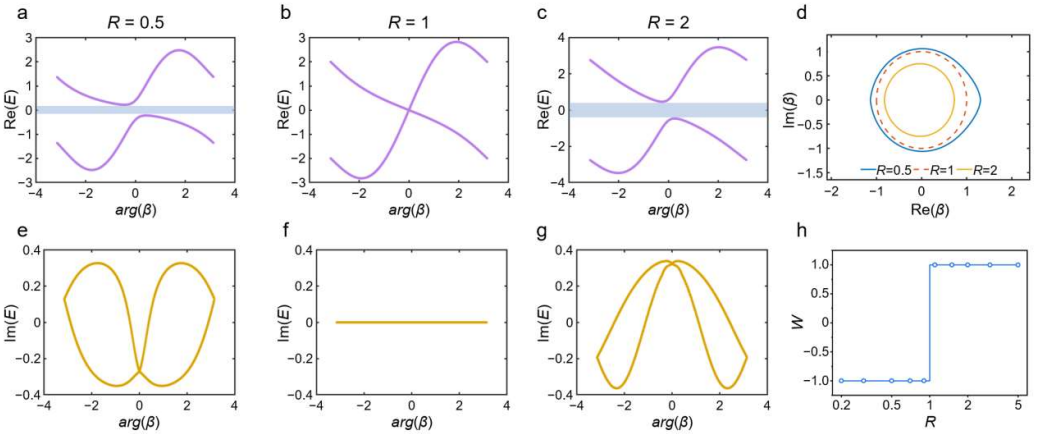

Figure 4. Band structure of thermal RPS Hamiltonian in GBZ. (a-c) Real part of

eigenvalues of $\mathbf{H}(k)$ with skewness $R = 0.5$, 1 and 2. (d) The GBZ of $\mathbf{H}(k)$ with skewness $R = 0.5$, 1 and 2. The dashed line is the unit circle (BZ, when $R = 1$). (e-g) Imaginary part of eigenvalues of $\mathbf{H}(k)$ with skewness $R = 0.5$, 1 and 2. (h) The topological invariant W of thermal RPS chain with different skewness R.

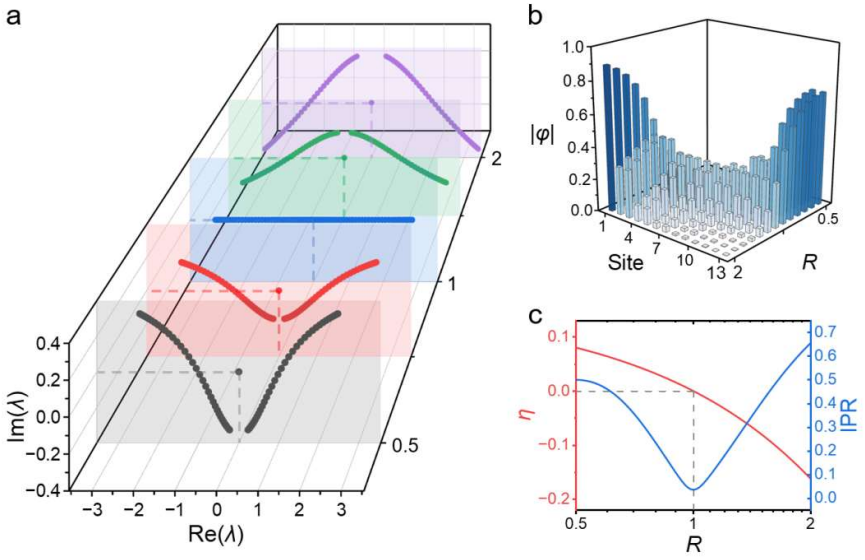

Figure 5. Eigenvalues and eigenvectors of finite thermal RPS chain under OBC. (a) Eigenvalues of real space Hamiltonian with different skewness (s = 81). (b) Eigenvectors corresponding to zero eigenvalues with different skewness (s = 13). (c) Normalized temperature deviation η and IPR under steady state with skewness varying from 0.5 to 2.